



Low onset potential on single crystal Ta₃N₅ polyhedron array photoanode with preferential exposure of {001} facets

Zhan Shi^{a,c}, Jianyong Feng^{a,b}, Hao Shan^{a,c}, Xin Wang^{a,b}, Zhe Xu^{a,b}, Huiting Huang^{a,b},
Qinfeng Qian^{a,b}, Shicheng Yan^{a,b,*}, Zhigang Zou^{a,b,c}

^a Collaborative Innovation Center of Advanced Microstructures, Nanjing University, Nanjing, 210093, PR China

^b Eco-materials and Renewable Energy Research Center (ERERC), National Laboratory of Solid State Microstructures, College of Engineering and Applied Science, Nanjing University, Nanjing 210093, PR China

^c Jiangsu Key Laboratory For Nano Technology, Department of Physics, Nanjing University, Nanjing, 210093, PR China

ARTICLE INFO

Keywords:

Ta₃N₅
polyhedron array
PEC water splitting
Solar energy conversion
Crystal facet engineering

ABSTRACT

The photoelectrochemical performance of photoanode depends significantly on the surface properties. Enormous efforts have been spent on fabricating photoanode with exposure of high-activity facets. However, precise control of the Ta₃N₅ facet exposure is still highly challenging, due to its harsh fabrication condition. In this study, it was found that Ta₃N₅ polyhedron can be grown through a bottom-up growth process in molten salt. Molten salt media in a semi-closed reactor provides a steady growth environment so that the Ta₃N₅ growth units are able to assemble in thermodynamically and kinetically favorable way. The preferential exposed facets are determined to be {001} facets. Due to the stronger built-in electric field on {001} facets and the small effective mass of hole along the [001] axis, an onset potential of 0.6 V versus reversible hydrogen electrode (RHE) and a photocurrent of 5.6 mA cm⁻² at 1.23 versus RHE have been achieved. Our findings may open an avenue to grow the nitride or oxynitride semiconductor crystals with desired structures for achieving efficient solar energy conversion and storage.

1. Introduction

Photoelectrochemical (PEC) water splitting is a potential approach to store intermittent and unequally distributed solar energy, on the basis of the separation of photogenerated charge by semiconductor-liquid junction (SCLJ) [1,2]. To raise energy conversion efficiency of PEC cell, a key challenge is to accelerate oxygen-evolving reaction (OER), a four-electron transfer process requiring high overpotentials [3]. A n-type semiconductor photoanode with high charge separation and strong oxidation capacity of holes is desired for challenging the OER kinetic limit. Usually, the hole extraction from the SCLJ is surface or/and interface-dependent. This probably is because the arrangement and coordination of atoms on different crystal facets lead to different electronic and chemical properties, which significantly influence the surface work function [4]. Several routes, such as passivating surface states, modifying a high-work-function layer, and exposing specific facets, have been developed to improve the built-in electric field at SCLJ interface, hence promoting the charge separation efficiency [5–14]. In addition, a nanostructured electrode exhibits high specific surface area, is more beneficial to enlarging the volume ratio of depletion region in

SCLJ, shorting charge diffusion distance to electrolyte and reducing bulk recombination [15,16].

Ta₃N₅ with band gap of about 2.1 eV, having maximum solar-to-hydrogen (STH) efficiency of 16%, is recognized to be one of the most promising photoanode materials [17,18]. However, the Ta₃N₅ photoanode still suffers from the relatively positive photocurrent onset potential at around 0.8–1.0 V versus reversible hydrogen electrode (RHE), which is 1.0–1.2 V far from the flat band potential of Ta₃N₅ (−0.2 V_{RHE}) [19]. Although element doping and/or surface modification are able to move the photocurrent onset potential to 0.6 V_{RHE}, thorough understanding of the origination of positive onset potentials of Ta₃N₅-based photoanodes still lacks [19–22]. Attempts to deliberately fabricate the single-crystal nanostructured electrodes are beneficial for discovering the factors that limited the PEC performance of Ta₃N₅. Although Ta₃N₅ with morphologies such as nanorod array and nanotube array was successfully fabricated, most of them are synthesized by nitriding tantalum oxide precursors via a pseudomorphic and topotactic phase transformation [20,23]. Replacing oxygen with nitrogen will lead to the changes of crystal structure and unit cell volume, so that this phase transformation is usually to produce porous structure or crystal defects.

* Corresponding author at: Collaborative Innovation Center of Advanced Microstructures, Nanjing University, Nanjing, 210093, PR China.
E-mail address: yscfen@nju.edu.cn (S. Yan).

<https://doi.org/10.1016/j.apcatb.2018.06.037>

Received 10 February 2018; Received in revised form 30 May 2018; Accepted 12 June 2018
Available online 18 June 2018

0926-3373/ © 2018 Elsevier B.V. All rights reserved.

This means that fabrication of nitride crystal film with exposure of specific facets is challenged by the thermodynamic growth mechanisms of the crystals.

Here, we successfully fabricated the Ta_3N_5 polyhedron array photoanode in the RbCl flux by using a semi-closed reactor to control the crystal growth. The single-crystal Ta_3N_5 polyhedron of about 400 nm in length and 150 nm in width formed via a nucleation and directional growth along the a -axis crystallographic direction to mainly expose the $\{001\}$ facets. The proposed crystal growth mechanism of Ta_3N_5 polyhedron, bottom-up assembling, can be extended to growing other tantalum nitrides or oxynitrides. The photoelectrochemical tests indicated that exposing $\{001\}$ facets is beneficial for extracting photo-generated holes to participate in OER, probably due to its inherently high surface band bending. The high Schottky barrier on the $\{001\}$ facets also makes the photo-generated electrons efficiently transport along the a -axis crystallographic direction to the conductive substrate. As a result, with the help of $\text{Ni}_{0.9}\text{Fe}_{0.1}\text{OOH}$ as an electrocatalyst to reduce the OER overpotentials, the Ta_3N_5 polyhedron photoanode with excellent charge separation afforded a low onset potential of about $0.6 V_{\text{RHE}}$ and 5.6 mA cm^{-2} photocurrent at 1.23 V versus reversible hydrogen electrode (RHE). Our results provided a new insight to understanding of the effects of crystal facet engineering on performance of PEC devices.

2. Experimental section

2.0.1. Fabrication of Ta_3N_5 photoanode

Ta foil (0.2 mm thickness) was cut into $0.7 \times 1.6 \text{ mm}^2$ pieces and washed ultrasonically with ethanol and acetone in succession for half an hour. Then, the Ta pieces were dried in air and annealed in muffle furnace in air at 550°C for 30 min. The oxidized Ta foils were put into Al_2O_3 boat for nitriding, with 1 g RbCl paved on. An Al_2O_3 cover was added to slow the flux draining rate. The boat was then transferred to a tube furnace for nitridation under 800 sccm NH_3 flow. The temperature ramped from room temperature to 850°C at a rate of 10°C per minute and kept for 300 min, then ramped to 950°C at a rate of 10°C per minute and kept for 100 min. After that, the tube was cooled down naturally, and then the Ta_3N_5 photoanodes were washed carefully with deionized water to remove the remaining flux. Other two sets of comparison samples were nitrided in an open Al_2O_3 boat with or without RbCl flux.

$\text{Ni}_{0.9}\text{Fe}_{0.1}\text{OOH}$ co-catalyst was deposited by electrodeposition method in a standard three-electrode system by potentiostatic method using an electrochemical analyzer (CHI-660, Shanghai Chenhua). The electrolyte contained 0.09 M $\text{Ni}(\text{NO}_3)_2 \cdot 6\text{H}_2\text{O}$ and 0.01 M $\text{Fe}(\text{SO}_4)_2 \cdot 7\text{H}_2\text{O}$. Ta_3N_5 photoelectrode was the work electrode, a Pt foil was the counter electrode and an Ag/AgCl electrode in saturated KCl solution was the reference electrode. The potential was kept at -0.5 V versus the reference electrode for 50 s. Photoassisted oxidation of Mn^{2+} was conducted in electrolyte containing 0.01 M MnSO_4 and 0.02 M KIO_3 (pH 4.5). The illumination time in photoassisted deposition was controlled to be 5 min. Photoassisted oxidation of Co^{2+} was conducted in 0.01 M $\text{Co}(\text{NO}_3)_2$ electrolyte (pH 4.8) for 30 min under illumination. A 300 mW Xe lamp was used as the light source here.

2.0.2. Characterization of samples

Crystal structure of the film was measured by X-ray diffraction (XRD, Rigaku, Ultima III, $\text{Cu K}\alpha$ irradiation). The morphology and cross-section images of photoanode were shot by field-emission scanning electron microscope (SEM, FEI Nova Nanosem 230). A transmission electron microscope (TEM, FEI TF-20) was used to record high resolution transmission electron microscope (HRTEM) images and selected area electron diffraction (SAED) images. An ultraviolet-visible spectrophotometer with integrating sphere (UV-VIS, Shimadzu UV-2550) was used to collect the wavelength-dependent light reflecting

spectra. The raw reflection data (R) was transferred into absorbance spectra (A) by the formula $A = 1 - R$.

2.0.3. Photoelectrochemical measurement

A standard three-electrode system, with Ta_3N_5 as working electrode, Pt foil as counter electrode and Ag/AgCl in saturated KCl as reference electrode, was utilized. Illumination was from an AM 1.5 G sunlight simulator (100 mW cm^{-2} , oriel 92251A-1000). A homemade light chopper was used to obtain the chopped J - V curves. An electrochemical analyzer (CHI-660, Shanghai Chenhua) was used to apply bias. The potential versus Ag/AgCl electrode ($V_{\text{Ag}/\text{AgCl}}$) was converted to potential versus reversible hydrogen electrode (V_{RHE}) by the formula $V_{\text{RHE}} = V_{\text{Ag}/\text{AgCl}} + 0.059 \times \text{pH} + 0.198 \text{ V}$. Hole injection efficiency was carried out in 1 M $\text{NaOH} + 0.1 \text{ M H}_2\text{O}_2$ electrolyte in the same condition. Electrochemical active surface was measured by cyclic voltammetry between -0.35 V to -0.1 V vs. Ag/AgCl in 1 M NaOH in the dark with altering scan rate. Relative electrochemical surface area of the photoanode is in proportional to the slope of the capacitive current-scan rate curve.

2.0.4. Computational details

Calculations in this work are performed using plane wave density function theory (DFT), as implemented in the Vienna Ab Initio Simulation Package (VASP), the generalized gradient approximations (GGA) in Perdew-Burke-Ernzerhof (PBE) with Heyd-Scuseria-Ernzerhof (HSE) method are employed as the exchange-correlation energy function. Parameters for the HSE calculation are $\alpha = 0.25$ and $\omega = 0.2 \text{ \AA}^{-1}$, which refer to the HSE06 functional. For the integration in the reciprocal space, a converged energy is reached for a k -point grid fineness of 0.05 eV \AA^{-1} . Cutoff energy for geometry optimization is 500 eV and the Brillouin zone integrations were $5 \times 5 \times 1$ k -point meshes. Supercell testing calculations were applied and the slab models were sufficient to obtain reliable results.

3. Results and discussion

3.1. Fabrication of Ta_3N_5 polyhedron photoanode

An Al_2O_3 boat with a cover on its top was used as a semi-closed reactor to grow the Ta_3N_5 crystal film. A Ta_2O_5 layer was pre-formed on the Ta substrate by directly heating Ta foil in air at 550°C for 30 min. The Ta foil with Ta_2O_5 layer was put into the semi-closed reactor. After covering the RbCl (1 g) on the Ta_2O_5 layer, the Ta_3N_5 crystal film was obtained at 850°C under flowing NH_3 (denoted as $\text{Ta}_3\text{N}_5\text{-C}$). For comparison, another two Ta_3N_5 samples were prepared by nitriding the pre-oxidized Ta plate with (denoted as $\text{Ta}_3\text{N}_5\text{-UC}$) or without (denoted as $\text{Ta}_3\text{N}_5\text{-T}$) addition of RbCl in an open Al_2O_3 boat, respectively.

X-ray diffraction (XRD) patterns indicate that the three as-prepared samples can be assigned to the orthorhombic Ta_3N_5 (JSPDS card No. 79-1533) (Fig. 1a). The XRD peaks of $\text{Ta}_{0.43}\text{N}$ are observed in all the three samples. The sub-nitride layer is well demonstrated to be a transition layer between Ta and Ta_3N_5 , which is probably a result of Ta diffusing into the Ta_3N_5 to form the Ta-rich phase during the nitriding [24]. The UV-vis absorption spectra (Fig. 1b) revealed that the three samples exhibited the main absorption edge at about 590 nm, originating from the electron transition from $\text{N}2\text{p}$ to $\text{Ta}5\text{d}$ [17]. Scanning electron microscope (SEM) observations show that the $\text{Ta}_3\text{N}_5\text{-T}$ is a polycrystalline film with a thickness of about 800 nm (Fig. 2a, b). The compact film consists of several-tens-of-nanometer irregular particles. $\text{Ta}_3\text{N}_5\text{-UC}$ has a composite structure, a 500-nm-thick compact irregular particle layer and a polyhedron (about 150 nm in length and 50 nm in width) array layer (Fig. 2c, d). The polyhedron presents a rectangular cross section along the crystal growth direction and two intersectant top-end facets. $\text{Ta}_3\text{N}_5\text{-C}$ presents the significantly narrowed compact

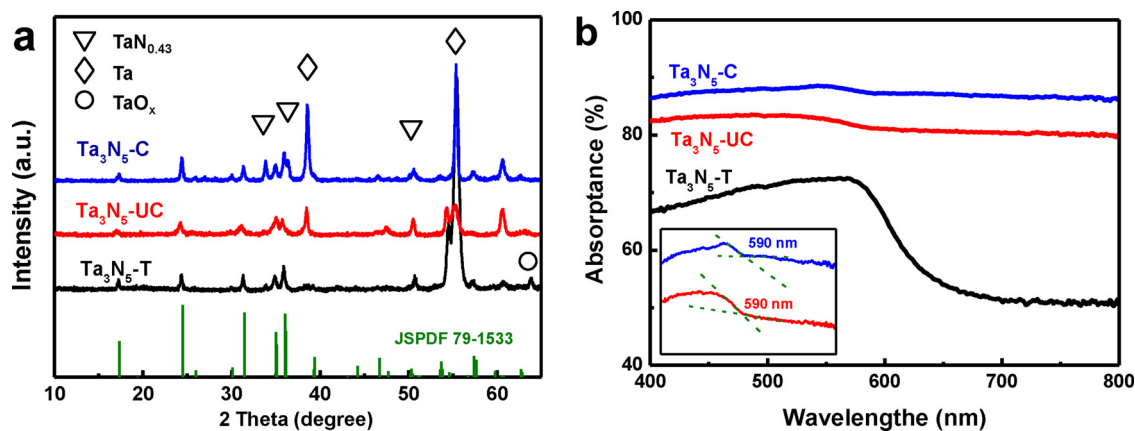


Fig. 1. a) XRD patterns of the Ta_3N_5 photoanodes. b) Light absorbance spectra of the Ta_3N_5 photoanodes. Inset shows the main band edge absorption for Ta_3N_5 -UC and Ta_3N_5 -C.

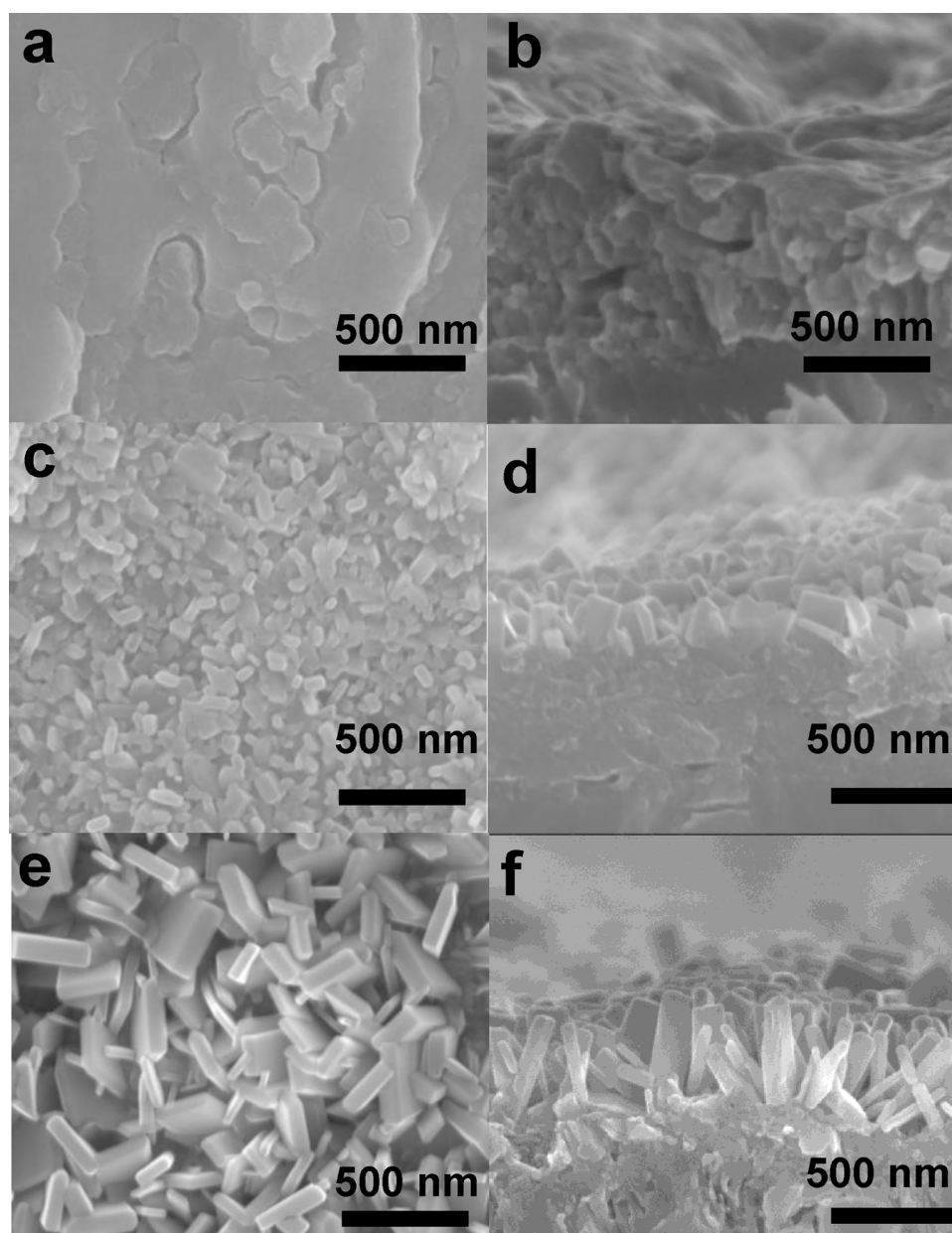


Fig. 2. Top-view and cross-section SEM images of Ta_3N_5 -T (a, b), Ta_3N_5 -UC (c, d), and Ta_3N_5 -C (e, f).

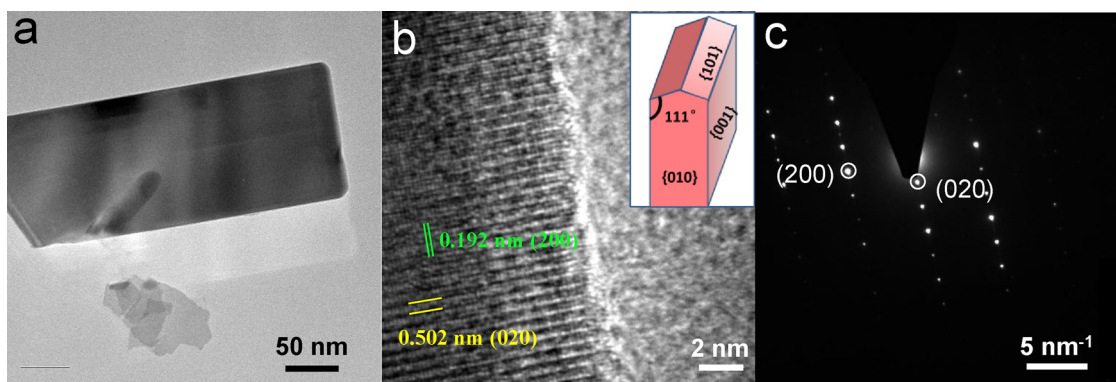


Fig. 3. TEM (a), HRTEM(b) and SAED (c) images of Ta_3N_5 -C polyhedron.

irregular particle layer (about 300 nm thickness) and evidently increased crystal size and density of single-crystal polyhedron (about 400 nm in length and 150 nm in width) array layer. (Fig. 2e, f) Energy dispersive X-ray spectroscopy (EDS) shows that the content of N and Ta is the same in the two layers, which demonstrates that both the two layers are Ta_3N_5 . (Figure S1)

To further investigate the nanostructure, the polyhedron of Ta_3N_5 -C was checked by transmission electron microscopy (TEM). As shown in Fig. 3a, two lattice fringes that are perpendicular to each other can be seen from the high resolution TEM (HRTEM) image. The longitude lattice fringe with 0.192 nm spacing and the latitude lattice fringe with 0.502 nm spacing are assigned to (200) and (020) planes of Ta_3N_5 , respectively. Thus, we can confirm that the Ta_3N_5 polyhedron with a rectangular cross section grew along the a -axis crystallographic direction. The two adjacent lateral surfaces parallel to the crystal growth direction are accordingly assigned to the {001} and {010} facets. The 111° interfacial angle between the top-end facet and {001} facet suggests that the top-end facet is {101} facets. Selected area electron diffraction (SAED) is well coincident with the HRTEM results and further confirmed that the Ta_3N_5 polyhedron is a well-grown single crystal.

3.2. Growth mechanism of the Ta_3N_5 polyhedron

It would be interesting to discover the growth mechanism of Ta_3N_5 polyhedron. Comparing the Ta_3N_5 -T and Ta_3N_5 -UC, it is obvious that the RbCl (melting point 718°C) as a molten salt is beneficial for the growth of Ta_3N_5 crystal, due to that the RbCl flux provided a liquid environment to accelerate the ion diffusion [25]. Growing the Ta_3N_5 in RbCl flux using an open boat produced a specific nanostructure that composed of the Ta_3N_5 polyhedron array on the dense Ta_3N_5 particle layer. The inhomogeneous polyhedrons with unsharp edge demonstrate that Ta_3N_5 nanocrystal is inadequately grown. This is probably attributed to the evaporation of RbCl at high temperature (850°C), inducing the unsteady liquid environment for single crystal growth. Indeed, lowering the reaction temperature to 800°C , polyhedrons with much clear facets and edges are obtained (Figure S2). To grow high-quality nanocrystal, the evaporation of solvent or the cooling of concentrated solution should be carefully controlled [26]. Gentle process allows the atoms to assemble in a thermodynamically and kinetically favorable way. Rapid destabilization often leads to disordered aggregation and defects. In addition, the TaO_x impurity is found in the Ta_3N_5 -T (Fig. 1a), meaning that the compact Ta_3N_5 particle layer suppressed the NH_3 diffusing into its bulk. No TaO_x impurity in Ta_3N_5 -UC and Ta_3N_5 -C demonstrates that the thinning of compact Ta_3N_5 layer facilitates the NH_3 infiltration.

To provide a steady-state growth environment, a cover was added on the Al_2O_3 boat. The cover is not air-tight, so that both NH_3 and RbCl vapor are able to permeate in and out. However, a vapor micro-circulation exists between the cover and the boat bottom, which

significantly decays the leaking rate of the NH_3 and RbCl, thus benefiting to achieve the balance between flux content and NH_3 diffusion. As a result, polyhedron that is similar with Ta_3N_5 -UC is produced, except that the crystal size increases for several folds.

The formation of Ta_3N_5 single crystal is believable to originate from a bottom-up growth instead of previously reported topotactic phase transformation from tantalum oxides. The importance of oxygen in the dissolving of tantalum has been emphasized [27]. Without the pre-oxidization step, Ta_3N_5 cannot be synthesized, meaning that the phase transformation from Ta_2O_5 into Ta_3N_5 is thermodynamically favorable compared to the direct reaction of Ta with N. After heating the pre-oxidized Ta_2O_5 film in RbCl flux under flowing Ar, it is visible that the morphology of recrystallized sample is completely different to the Ta_3N_5 polyhedron (Figure S3a and Fig. 4a). XRD pattern indicated that the recrystallized sample still is Ta_2O_5 , suggesting that the Ta_2O_5 precursor is able to dissolve into the RbCl flux. Meanwhile, the Ta_3N_5 polyhedron can be grew by recrystallization of the Ta_3N_5 -T in the presence of RbCl flux (Fig. 4b). These evidences illustrate that the Ta_3N_5 crystal growth starts from the dissolving of the tantalum compounds (TaO_x or Ta_xN_x) into RbCl flux, and subsequently driven by supersaturation, the growth units assemble into well-shaped polyhedron crystals. Such a bottom-up crystal growth mechanism prevents the formation of pores and defects that would happen in topotactic phase transformation due to changes of cell volume.

Polyhedron shape is determined by both thermodynamics and growth kinetics. Facets with low surface energy and low growth rate will finally expose. Changing surface energy by specific ion adsorption is a well-established method to control crystal shape [9]. At high temperature, RbCl flux will partly ionize into Rb^+ and Cl^- . The long axis of the polyhedron here also orients in [100] direction. It implies that Cl^- ions lead to preferential growth of [100] direction in this case, as well demonstrated in the needlelike Ta_3N_5 growing along [100] direction by using TaCl_5 and NH_4Cl as precursors [28]. Altering the flux to RbBr, large rectangular {001} facet dominated Ta_3N_5 sheet without preferential growth direction is produced (Fig. 4c). The result also illustrates that Rb^+ ion may decrease the surface energy of {001} facets or slow the crystal growth rate on {001} facets, leading to the final preferential exposure. Substituting RbCl with KBr will produce a dense Ta_3N_5 film composed of irregular nanoparticles (Fig. 4d). Therefore, it is a dependable conclusion that the co-adsorption of Cl^- and Rb^+ determines the directional growth of Ta_3N_5 polyhedron. These evidences would indicate that the flux-assisted bottom-up crystal growth mechanism provides a possibility to engineering the exposure of specific facets for nitrides by using the specific adsorbed ions.

3.3. PEC performance of the photoanodes

The PEC water splitting performance of these as-prepared samples was checked under AM 1.5 G simulated sunlight irradiation in 1 M

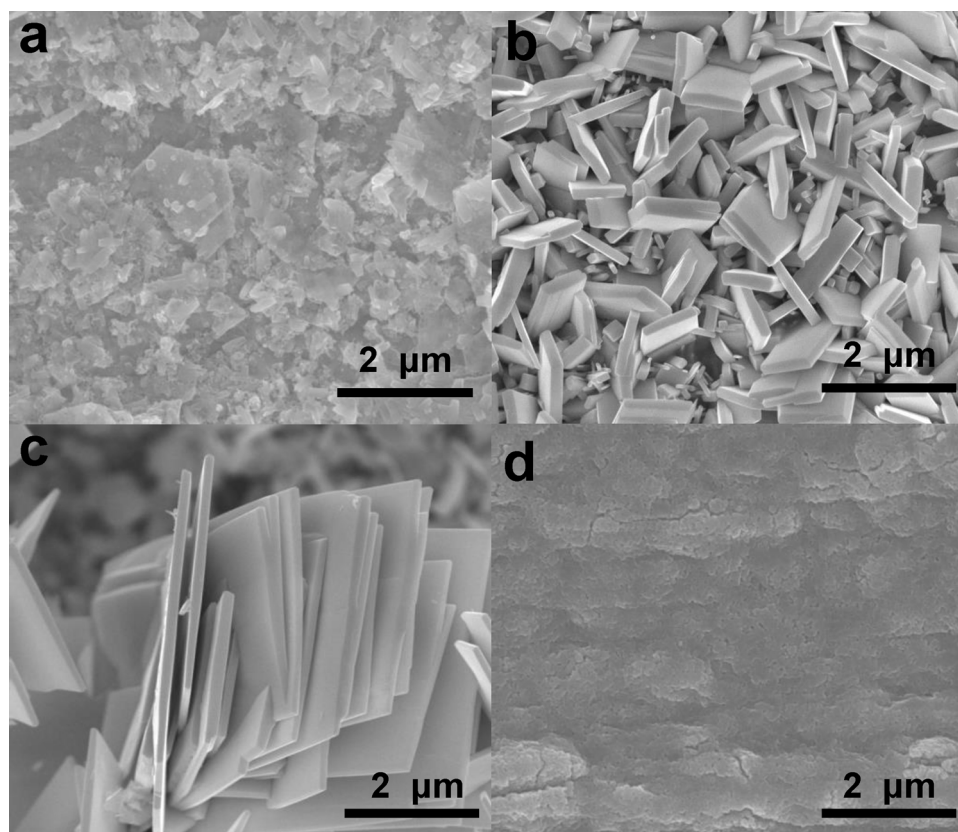


Fig. 4. SEM images for the recrystallized Ta_2O_5 in RbCl flux under Ar atmosphere (a), the recrystallized Ta_3N_5 in RbCl flux under NH_3 (b), and Ta_3N_5 obtained by nitriding the pre-oxidized Ta_2O_5 film in RbBr flux (c) or in KBr flux (d).

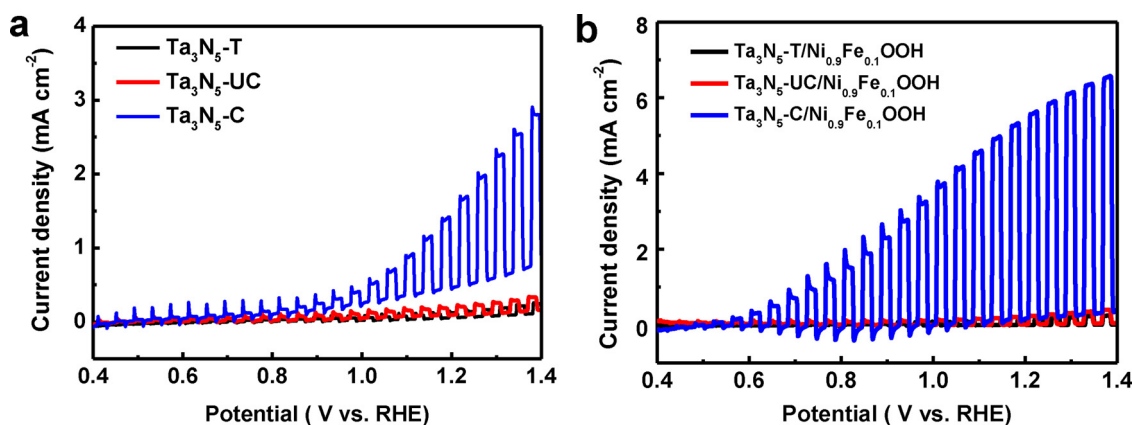


Fig. 5. Chopped-light photocurrent-potential curves for bare Ta_3N_5 photoanodes (a) and $\text{Ni}_{0.9}\text{Fe}_{0.1}\text{OOH}/\text{Ta}_3\text{N}_5$ photoanodes (b). The scan rate is 30 mV s^{-1} .

NaOH electrolyte (pH 13.6). The saturated photocurrent on $\text{Ta}_3\text{N}_5\text{-T}$ photoanode is below 0.2 mA cm^{-2} (Fig. 5a). It probably results from that the topotactic phase transformation from the Ta_2O_5 to Ta_3N_5 produced the crystal defects, which can act as the charge recombination center [18]. A slight increase in saturated photocurrent of $\text{Ta}_3\text{N}_5\text{-UC}$ would be attributed to the formation of Ta_3N_5 polyhedron layer. Indeed, the $\text{Ta}_3\text{N}_5\text{-C}$ photoanode with well-grown polyhedron array exhibited the saturated photocurrent increase by more than one order of magnitude. The increased dark current of $\text{Ta}_3\text{N}_5\text{-C}$ photoanode may be ascribed to the re-oxidation of the sub-nitride layer [29]. Loading co-catalysts is indispensable for Ta_3N_5 photoanode to overcome the sluggish OER kinetics to get satisfying photocurrent (Figure S3). After the loading of $\text{Ni}_{0.9}\text{Fe}_{0.1}\text{OOH}$, which is among the most effective OER catalyst [30], the photocurrents of both $\text{Ta}_3\text{N}_5\text{-T}$ and $\text{Ta}_3\text{N}_5\text{-UC}$ did not improve obviously. In contrast, the performance of $\text{Ta}_3\text{N}_5\text{-C}$ is further

promoted to an impressive value. The onset potential moves to around $0.6 V_{\text{RHE}}$, and the current density at $1.23 V_{\text{RHE}}$ is about 5.6 mA cm^{-2} .

For PEC water splitting, the photocurrent (J) is determined by light absorption (J_{abs}), charge separation efficiency (η_{sep}) and surface injection efficiency (η_{inj}), as described in Eq. (1) [2].

$$J = J_{\text{abs}} \times \eta_{\text{sep}} \times \eta_{\text{inj}} \quad (1)$$

To explore the major factor that contributes to the superior PEC performance of $\text{Ta}_3\text{N}_5\text{-C}$, the three components were individually extracted. Here, due to lacking of transmission on the Ta substrate, absorbance (A) can be figured, once the reflection (R) is measured, by Eq. (2).

$$A(\lambda) = 1 - R(\lambda) \quad (2)$$

Then J_{abs} can be figured out by integrating the product of $A(\lambda)$ and

incident photon intensity ($I_0(\lambda)$) of AM 1.5 G simulated sunlight, according to Eq. (3) (E_g is the band edge of semiconductor).

$$J_{abs} = \int_0^{1240/E_g} A(\lambda) I_0(\lambda) d\lambda \quad (3)$$

The low absorption coefficient ($\sim 10^4 \text{ cm}^{-1}$ from 400 to 600 nm) has always been a problem to be solved for Ta_3N_5 [24,31]. It is estimated that a planar Ta_3N_5 film of micron-scale-thick is necessary to capture most of the incident photons, due to the severe reflection and short light absorption path length. It can be seen from Fig. 1b that the absorbance of planar Ta_3N_5 -T is only around 70% from 400 nm to 600 nm. Increasing the thickness of planar Ta_3N_5 film to enhance the absorption will then increase the charge carrier transport distance [32]. The conflict is successfully resolved by the fabrication of the polyhedron array. The Ta_3N_5 polyhedron array remarkably increased the light penetration depth, suppressed reflection and enhanced light scattering. Consequently, the absorbance of Ta_3N_5 -C increased to over 85% in the range of 400–800 nm without increasing the thickness of Ta_3N_5 . However, with enhanced light capturing ability, photocurrent of Ta_3N_5 -UC is not significant. Besides, the integral J_{abs} of the photoanodes are close to each other (Figure S6). Thus, the enhancement of light absorption is not the major factor for the photocurrent difference between Ta_3N_5 -C and Ta_3N_5 -UC photoanodes.

To calculate the hole injection efficiency, the photocurrents were measured with the existence of hole sacrificial agent, where the hole injection efficiencies of the photoanodes can be regarded as unit (Fig. 6). In the presence of H_2O_2 , the PEC performances of $\text{Ni}_{0.9}\text{Fe}_{0.1}\text{OOH}/\text{Ta}_3\text{N}_5$ -UC and $\text{Ni}_{0.9}\text{Fe}_{0.1}\text{OOH}/\text{Ta}_3\text{N}_5$ -T did not enhance obviously. Therefore, their poor photocurrent cannot be ascribed to their low hole injection efficiencies. The photocurrent of $\text{Ni}_{0.9}\text{Fe}_{0.1}\text{OOH}/\text{Ta}_3\text{N}_5$ -C enhances significantly, except that the onset potential shifted cathodically to about 0.5 V_{RHE} . Hole injection efficiency can be calculated by

$$\eta_{inj} = J_{\text{H}_2\text{O}}/J_{\text{H}_2\text{O}_2} \quad (4)$$

At 1.23 V_{RHE} , the η_{inj} of Ta_3N_5 -C is around 90%, while those of Ta_3N_5 -T and Ta_3N_5 -UC are similar to be around 70%. It illustrates that most of the photogenerated holes that reach the interface are consumed by PEC reaction. However, the 20% improvement of η_{inj} cannot afford the about 28 times photocurrent increment for Ta_3N_5 -C (5.6 mA cm^{-2} at 1.23 V_{RHE}) than Ta_3N_5 -UC ($< 0.2 \text{ mA cm}^{-2}$ at 1.23 V_{RHE}).

Ruling out the mentioned-above two factors, it turns out that the charge separation efficiency is the decisive factor. According to Eq. (1), it can be calculated that at 1.23 V_{RHE} , η_{sep} of Ta_3N_5 -C is approximate 20 times larger compared to those of Ta_3N_5 -UC and Ta_3N_5 -T (Fig. 7a). The drifting of photogenerated holes is driven by the built-in electric field within space charge layer. The construction of nanostructured morphology apparently enlarges the interface area of SCLJ, which increases the volume ratio of the space charge layer and shortens the necessary migration distance. Although it is difficult to figure out the true value of the SCLJ interface area, the relative electrochemical surface area (S_{EC}) can be calculated from the capacitive current-scan rate curve, in which

S_{CE} is directly proportional to the slope [33]. S_{CE} of Ta_3N_5 -C is determined to be about 9 times larger than that of the planar Ta_3N_5 -T or Ta_3N_5 -UC (Fig. 7b). Dividing η_{sep} by S_{EC} , the separation efficiency per S_{EC} for Ta_3N_5 -C ($5.4\% S_{\text{EC}}^{-1}$) is still more than two times higher than that for Ta_3N_5 -T ($1.9\% S_{\text{EC}}^{-1}$). It demonstrates that besides the enlarged space charge layer ratio, there are some intrinsic properties of Ta_3N_5 -C that improve the charge separation efficiency.

To further explore the reasons that make Ta_3N_5 -C photoanode superior, deposition of MnO_x on Ta_3N_5 -C via photoassisted oxidation of Mn^{2+} ion was carried out, where Mn^{2+} worked as an indicator of the photogenerated holes. Seen from the SEM image, the sponge-like manganese oxide selectively deposited on the {001} facets and {010} facets, not appearing on {101} facets (Fig. 8a). Also, photooxidation of cobalt selectively occurred on {001} and {010} facets (Fig. 8b). The result reveals that the photogenerated holes transport to and accumulate on {001} and {010} facets, making the two facets advantageous for photooxidation reactions. Similar phenomenon is also found in other photoanode materials such as BiVO_4 and TiO_2 [10,13,34]. Photooxidation selectively occurs on the {110} facets of BiVO_4 and {001} facets of TiO_2 , while photoreduction selectively occurs on the {001} facets of BiVO_4 and {101} facets of TiO_2 . The fundamental principle of the charge carrier accumulation is still under debate. One prevailing hypothesis is that the strength of built-in electric field within SCLJ is the determining factor [12,34]. Facets with stronger built-in electric field are the oxidation facets due to the enhanced carrier drifting. The surface work function describes the surface band bending. Therefore, a density function theory (DFT) calculation of a slab model was carried out to get the surface work function. The surface work function of (101) facet is about 4.40 eV, which is about 0.20 eV smaller than that of (001) facet and 0.26 eV smaller than that of (010) facet (Fig. 8). The calculated result matches well with the photooxidation experiment results. It demonstrates that the driven force of holes to the semiconductor-electrolyte interface and electrons to the conductive substrate is enhanced for the {001} and {010} facets. In addition, the mobility difference of charge carrier along different crystallographic axes should also be taken into account [35]. It has been predicted that the effective mass of hole, which is inversely proportional to the mobility, is significantly smaller along [001] axis and the effective mass of electron is smaller along [100] axis ($m_h = 0.26m_0$ along [001] axis and $m_e = 0.21m_0$ along [100] axis) [36]. It also favors the charge migration in the polyhedron shaped nanocrystal. Consequently, preferentially growing the Ta_3N_5 along [100] axis and exposing {001} facets are advantageous to the charge separation and transport, thus improving the PEC performance of Ta_3N_5 photoanodes.

4. Conclusion

In summary, Ta_3N_5 polyhedron array photoanode with preferential exposure of {001} facets was fabricated via a template-free, non-toxic and facile molten salt method. It was well demonstrated that the formation of Ta_3N_5 polyhedron follows a bottom-up crystal growth

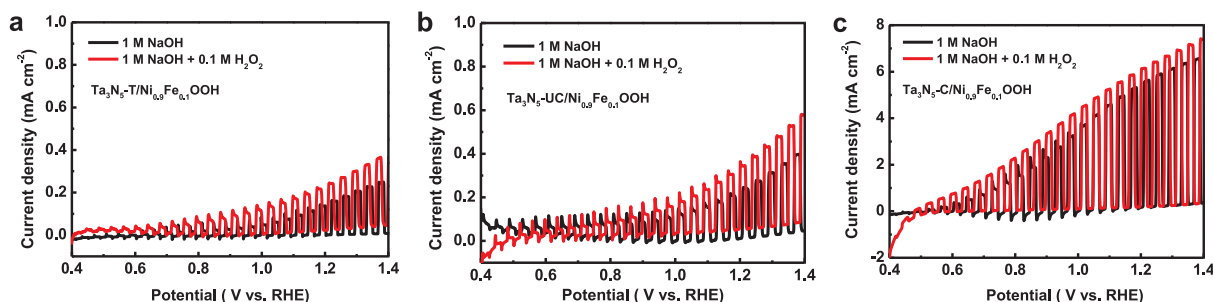


Fig. 6. Chopped-light photocurrent-potential curves of the $\text{Ni}_{0.9}\text{Fe}_{0.1}\text{OOH}$ loaded Ta_3N_5 -T (a), Ta_3N_5 -UC (b), Ta_3N_5 -C (c) in 1 M NaOH electrolyte and 1 M NaOH + 0.1 M H_2O_2 mixed electrolyte.

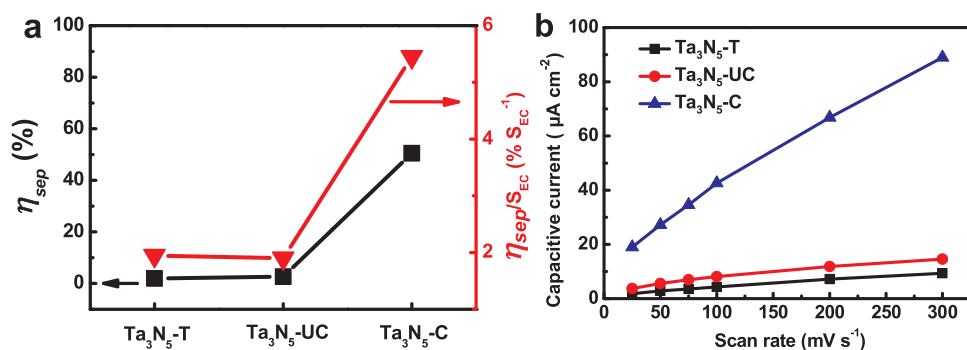


Fig. 7. a) The calculated results of the charge separation efficiency and charge separation efficiency per relative electrochemical surface area at 1.23 V_{RHE}. Electrochemical surface area of Ta₃N₅-T is defined as unit. Detailed data is listed in Table S1. b) Capacitive current-scan rate curves of the Ta₃N₅ photoanodes.

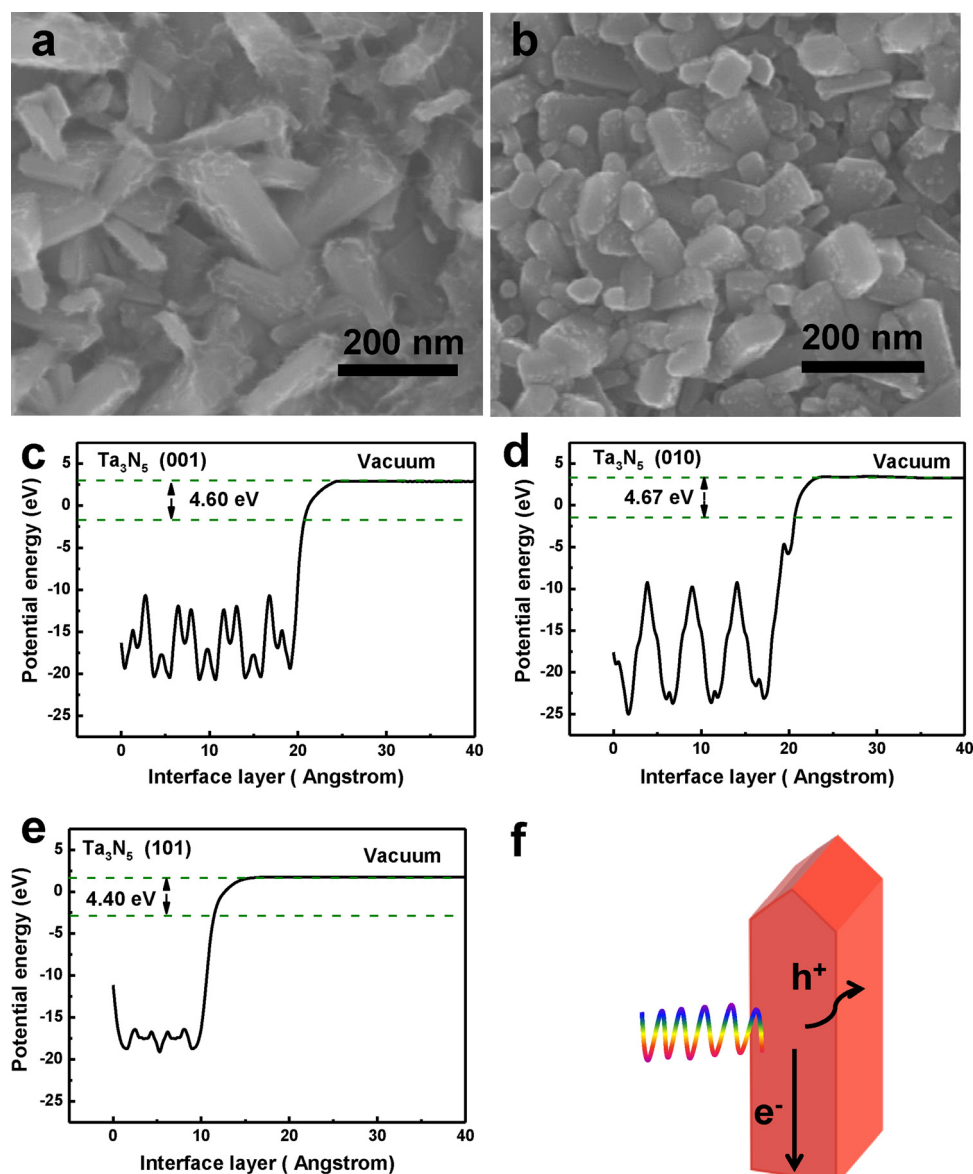


Fig. 8. SEM images of photo-assisted oxidation of Mn²⁺ (a) and Co²⁺ (b) on Ta₃N₅-C photoanode. Surface potential energy-interface layer curves of (001) facet (c), (010) facet (d) and (101) facet (e) obtained from DFT calculation. (f) Schematic diagram of anisotropic charge separation in Ta₃N₅ polyhedron.

mechanism, implying that it is possible to grow a nitride crystal with desired structures if deeply selected the appropriate growth environment and adsorbed ions. An onset potential of 0.6 V_{RHE} and a current density of 5.61 mA cm⁻² at 1.23 V_{RHE} were achieved on the Ta₃N₅

polyhedron array photoanode. The superior PEC performance originates from stronger built-in electric field on {001} facets and the small effective mass of hole along the [001] axis. The result exhibits the bright future in facet engineering for Ta₃N₅ photoanode. Due to the

similar growing conditions, the bottom-up crystal growth mechanism is not only instructive for Ta₃N₅, but also for a vast variety of nitrides or oxynitrides.

Acknowledgements

This work was supported primarily by the National Basic Research Program of China (2013CB632404), the National Natural Science Foundation of China (51572121, 21603098, and 21633004), the Natural Science Foundation of Jiangsu Province (BK20151265, BK20151383, and BK20150580), the Postdoctoral Science Foundation of China (2017M611784), the Fundamental Research Funds for the Central Universities (021314380133 and 021314380084), and the program B for Outstanding PhD candidate of Nanjing University (201702B084). We are grateful to the High Performance Computing Center (HPCC) of Nanjing University for doing the numerical calculations in this paper on its IBM Blade cluster system.

Appendix A. Supplementary data

Supplementary material related to this article can be found, in the online version, at doi:<https://doi.org/10.1016/j.apcatb.2018.06.037>.

References

- [1] A. Fujishima, K. Honda, *Nature* 238 (1972) 37–38.
- [2] M.G. Walter, E.L. Warren, J.R. McKone, S.W. Boettcher, Q. Mi, E.A. Santori, N.S. Lewis, *Chem. Rev.* 110 (2010) 6446–6473.
- [3] M.W. Kanan, D.G. Nocera, *Science* 321 (2008) 1072–1075.
- [4] A.L. Linsebigler, G. Lu, J.T. Yates Jr, *Chem. Rev.* 95 (1995) 735–758.
- [5] F. Le Formal, N. Tétreault, M. Cornuz, T. Moehl, M. Grätzel, K. Sivula, *Chem. Sci.* 2 (2011) 737–743.
- [6] Z. Xu, Z. Fan, Z. Shi, M. Li, J. Feng, L. Pei, C. Zhou, J. Zhou, L. Yang, W. Li, G. Xu, S. Yan, Z. Zou, *ChemSusChem* 11 (2018) 237–244.
- [7] M.J. Kenney, M. Gong, Y. Li, J.Z. Wu, J. Feng, M. Lanza, H. Dai, *Science* 342 (2013) 836–840.
- [8] G. Xu, Z. Xu, Z. Shi, L. Pei, S. Yan, Z. Gu, Z. Zou, *ChemSusChem* 10 (2017) 2897–2903.
- [9] H.G. Yang, C.H. Sun, S.Z. Qiao, J. Zou, G. Liu, S.C. Smith, H.M. Chen, G.Q. Lu, *Nature* 453 (2008) 638–641.
- [10] J. Yu, J. Low, W. Xiao, P. Zhou, M. Jaroniec, *J. Am. Chem. Soc.* 136 (2014) 8839–8842.
- [11] P. Li, Y. Zhou, Z. Zhao, Q. Xu, X. Wang, M. Xiao, Z. Zou, *J. Am. Chem. Soc.* 137 (2015) 9547–9550.
- [12] L. Wang, J. Ge, A. Wang, M. Deng, X. Wang, S. Bai, R. Li, J. Jiang, Q. Zhang, Y. Luo, Y. Xiong, *Angew. Chem.* 126 (2014) 5207–5211.
- [13] R. Li, F. Zhang, D. Wang, J. Yang, M. Li, J. Zhu, X. Zhou, H. Han, C. Li, *Nat. Commun.* 4 (2013) 1432.
- [14] L. Mu, Y. Zhao, A. Li, S. Wang, Z. Wang, J. Yang, Y. Wang, T. Liu, R. Chen, J. Zhu, F. Fan, R. Li, C. Li, *Energy Environ. Sci.* 9 (2016) 2463–2469.
- [15] X. Zhao, W. Luo, J. Feng, M. Li, Z. Li, T. Yu, Z. Zou, *Adv. Energy Mater.* 4 (2014) 1301785.
- [16] J. Feng, W. Luo, T. Fang, H. Lv, Z. Wang, J. Gao, W. Liu, T. Yu, Z. Li, Z. Zou, *Adv. Funct. Mater.* 24 (2014) 3535–3542.
- [17] G. Hitoki, A. Ishikawa, T. Takata, J.N. Kondo, M. Hara, K. Domen, *Chem. Lett.* 31 (2002) 736–737.
- [18] M. Li, W. Luo, D. Cao, X. Zhao, Z. Li, T. Yu, Z. Zou, *Angew. Chem. Int. Ed.* 52 (2013) 11016–11020.
- [19] J. Seo, T. Takata, M. Nakabayashi, T. Hisatomi, N. Shibata, T. Minegishi, K. Domen, *J. Am. Chem. Soc.* 137 (2015) 12780–12783.
- [20] Y. Li, L. Zhang, A. Torres-Pardo, J.M. González-Calbet, Y. Ma, P. Oleynikov, O. Terasaki, S. Asahina, M. Shima, D. Cha, L. Zhao, K. Takanabe, J. Kubota, K. Domen, *Nat. Commun.* 4 (2013) 2566.
- [21] S. Chen, S. Shen, G. Liu, Y. Qi, F. Zhang, C. Li, *Angew. Chem. Int. Ed.* 54 (2015) 3047–3051.
- [22] G. Liu, S. Ye, P. Yan, F. Xiong, P. Fu, Z. Wang, Z. Chen, J. Shi, C. Li, *Energy Environ. Sci.* 9 (2016) 1327–1334.
- [23] X. Feng, T.J. LaTempa, J.I. Basham, G.K. Mor, O.K. Varghese, C.A. Grimes, *Nano Lett.* 10 (2010) 948–952.
- [24] B.A. Pinaud, A. Vailionis, T.F. Jaramillo, *Chem. Mater.* 26 (2014) 1576–1582.
- [25] P. Afanasiev, C. Geantet, *Coord. Chem. Rev.* 178 (1998) 1725–1752.
- [26] L. Wu, J.J. Willis, I.S. McKay, B.T. Diroll, J. Qin, M. Cargnello, C.J. Tassone, *Nature* 548 (2017) 197–201.
- [27] S. Suzuki, H. Wagata, M. Komatsu, T. Minegishi, K. Domen, S. Oishi, K. Teshima, *J. Mater. Chem. A* 3 (2015) 13946–13952.
- [28] D. Lu, M. Hara, T. Hisatomi, T. Takata, K. Domen, *J. Phys. Chem. C* 113 (2009) 17151–17155.
- [29] L. Wang, X. Zhou, N.T. Nguyen, I. Hwang, P. Schmuki, *Adv. Mater.* 28 (2016) 2432–2438.
- [30] L. Trotochaud, S.L. Young, J.K. Ranney, S.W. Boettcher, *J. Am. Chem. Soc.* 136 (2014) 6744–6753.
- [31] J.M. Morbec, I. Narkeviciute, T.F. Jaramillo, G. Galli, *Phys. Rev. B* 90 (2014) 155204.
- [32] I.S. Cho, Z. Chen, A.J. Forman, D.R. Kim, P.M. Rao, T.F. Jaramillo, X. Zheng, *Nano Lett.* 11 (2011) 4978–4984.
- [33] B.A. Pinaud, P.C.K. Vesborg, T.F. Jaramillo, *J. Phys. Chem. C* 116 (2012) 15918–15924.
- [34] J. Zhu, F. Fan, R. Chen, H. An, Z. Feng, C. Li, *Angew. Chem. Int. Ed.* 54 (2015) 9111–9114.
- [35] T. Liu, X. Zhou, M. Dupuis, C. Li, *Phys. Chem. Chem. Phys.* 17 (2015) 23503–23510.
- [36] J.M. Morbec, G. Galli, *Phys. Rev. B* 93 (2016) 035201.